Journal of Materials Science: Materials in Electronics (2018) 29:20206–20215
https://doi.org/10.1007/s10854-018-0153-3

Impedance spectroscopy and magnetic properties of Mg doped Y-type barium hexaferrite

Pratap Behera[1] · **S. Ravi**[1]

Received: 12 March 2018 / Accepted: 4 October 2018 / Published online: 6 October 2018

Abstract

Single phase samples of Mg doped Y-type hexaferrites with a composition of $Ba_2(Co_{1-x}Mg_x)_2Fe_{12}O_{22}$ for $x = 0–0.5$ were prepared using the solid state route. The values of lattice constant and the unit cell volume are found to decrease systematically with increase in Mg concentration. The analysis of impedance spectra and the thermal activation of relaxation process show the contributions from both grains and grain boundaries with decrease in activation energies as Mg concentration is increased. The complex impedance spectra show a deviation from an ideal Debye type and they are modelled using an equivalent circuit consisting of resistances of grains and grain boundaries, grain capacitance and a constant phase element. However at higher temperature ($T \geq 573$ K), the contribution of electrode resistance is also taken into account. The analysis of electrical conductivity data show that it is controlled by small polaron tunneling model. The magnetization measurements show that the saturation magnetization marginally decreases from 26.6 emu/g for $x = 0$–22.7 emu/g for $x = 0.5$ along with decrease in ferrimagnetic transition temperature from 613 to 581 K.

1 Introduction

Y-type hexaferrites, $Ba_2Me_2Fe_{12}O_{22}$ (Me = Co, Ni, Zn, etc.) continue to draw the research interest due to their potential applications as electronic devices in the area of telecommunication [1–3]. Y-type hexaferrites are the first ferroxplana ferrites in the hexagonal family i.e. having the easy plane of magnetization perpendicular to the c-axis and they exhibit excellent magnetic properties in the high frequency region. Since the Y-type hexaferrites have magnetic planar anisotropy, the cut off frequency is very much higher than that of spinel ferrites and garnets. Thus, these materials are natural choice for applications in the high frequency range [4, 5]. The Y-type hexaferrite consists of alternate stacking of three spinel (S)-blocks and three tetrahedral (T)-blocks along the c-axis [6–8]. Both Fe^{3+} ions and the metallic cations are distributed over the six interstitial sites with $3a_{vi}(\uparrow)$, $3b_{vi}(\uparrow)$ and $18h_{vi}(\uparrow)$ in spin up state and $6c_{vi}(\downarrow)$, $6c_{iv}(\downarrow)$ and $6c_{iv*}(\downarrow)$ in the spin down state respectively. Therefore, the substitution of suitable metal ions for Fe or Co may lead to interesting magnetic properties in Co_2Y hexaferrite.

Some of the Y-type barium hexaferrites, such as $Ba_2Mg_2Fe_{12}O_{22}$, $Ba_{0.5}Sr_{1.5}Zn_2Fe_{12}O_{22}$, $Ba_{0.5}Sr_{1.5}Co_2Fe_{12}O_{22}$ are found to exhibit magneto-electric coupling at low temperatures for low magnetic fields [9–11]. The partial substitution of non-magnetic Al^{3+} ion in $Ba_2Co_2Fe_{12}O_{22}$ (Co_2Y) hexaferrites gives rise to magneto-electricity at room temperature [12]. Magneto-electric effect can also be obtained with different cationic substitutions in Y-type hexaferrites [11, 13]. The magneto-electric effect is one of the important properties of Y-type hexferrites which basically arises due to the ferroelectric polarization induced by their spiral magnetic structure. The oxygen annealing of $BaSrCo_2Fe_{11}AlO_{22}$ samples under high pressure is reported to show magneto-electric (ME) behavior at room temperature [14]. Costa et al. have shown that Co_2Y hexaferrites exhibit excellent dielectric, impedance and conductivity behavior at different temperatures which are important properties for microwave applications [15]. Farzin et al., have reported that substitution of Ni^{2+} and Mg^{2+} ions have large influence on the microstructure and magnetic properties of Co_2Y hexaferrite [16]. The cationic distribution of non-magnetic Mg^{2+} ions at Co^{2+} site in other hexaferrites is found to exhibit excellent magnetic, dielectric and electrical properties with an ability to tune the planar anisotropy [17, 18]. The substitution of Mg^{2+} ions at Co^{2+} site in W-type hexaferrite gives rise to better magnetization values and they are found to be suitable for microwave absorption and electromagnetic

---

✉ S. Ravi
sravi@iitg.ac.in

[1] Department of Physics, Indian Institute of Technology Guwahati, Guwahati 781039, India

interference attenuations [17]. The dielectric and magnetic properties of Y-type hexaferrites also depend strongly on the method of preparation, distribution of cations at various sites and their substitution by other relevant elements. The study of frequency variation of dielectric constant and impedance spectroscopy generally provide the relevant information to understand the conduction process in a dielectric material. The contribution of grains, grain boundaries and the electrode effects towards the electrical conduction, polarization and the dielectric relaxation can be understood from the impedance analysis. In view of the comparable ionic sizes of Mg^{2+} and Co^{2+} ions and the interesting properties of Mg substitution in other hexaferrites, we have systematically investigated the effect of Mg ion substitution on microstructure, magnetic, impedance and conductivity behavior of Co_2Y hexaferrite.

2 Experimental details

$Ba_2(Co_{1-x}Mg_x)_2Fe_{12}O_{22}$ ($0 \le x \le 0.5$) samples were prepared by using the solid state reaction technique. High purity (> 99%) $BaCO_3$, Fe_2O_3, MgO, and Co_3O_4 powders were taken as starting compounds. Stoichiometric molar ratios of starting compounds were weighed and grinded together in acetone medium for 3 h using agate mortar and pestle. The above mixed powders were presintered at 600 °C for 12 h. The presintered powders were pressed into cylindrical pellets of diameter ~ 13 mm using a hydraulic press with a pressure of 2.9×10^8 N/m^2 and the final annealing was carried out at 1150 °C for 12 h in the air medium. X-ray diffraction (XRD) patterns were recorded using Rigaku make TTRAX III X-ray diffractometer with CuK$_\alpha$ radiation ($\lambda = 1.54056$ Å) and analysis of these XRD patterns were carried out by Rietveld refinement technique with the help of Fullprof software [19]. The surface morphology and the compositional analysis were checked by using ZEISS make field emission scanning electron microscope (Model. Sigma) and using the energy dispersive X-ray spectroscopic technique (EDX). Temperature and field dependent magnetization measurements were carried out by using LakeShore make vibrating sample magnetometer (VSM, model no. 7410). The dielectric measurements were performed at different temperatures in the frequency range of 10^2–10^6 Hz by using Wayne Kerr make LCR meter of model no. 4300. Silver paint was used on both side of the sample as electrodes.

3 Results and discussions

Typical XRD patterns of $x = 0$ and 0.5 samples of $Ba_2(Co_{1-x}Mg_x)_2Fe_{12}O_{22}$ are shown in Fig. 1. These patterns were analyzed based on R-3m space group and the refined data are shown as solid lines in Fig. 1. As per the Rietveld refinement, all the observed peaks are accounted within the R-3m space group and it confirms that the prepared materials are in single-phase form with rhombohedral structure. Similar refining was carried out for all other samples in this series. The determined lattice parameters in hexagonal coordinates are found to be $a = 5.862$ Å and $c = 43.512$ Å for $x = 0$. The lattice constant c is found to decrease systematically with increase in Mg concentration as shown in Table 1. These lattice parameters are comparable to those of Mg substituted $Ba_{0.5}Sr_{1.5}Zn_2Fe_{12}O_{22}$ hexaferrites [4, 20]. The unit cell volume determined from the above analysis is found to decrease with increase in Mg concentration, as shown in Table 1. The decrease in lattice parameter c and the unit cell volume with respect to Mg concentration can be attributed to the substitution of smaller Mg^{2+} (0.72 Å) ions at Co^{2+} (0.745 Å) site [21, 22].

The microstructural images of all the samples were recorded by using field emission scanning electron microscope (FESEM) and their typical images for $x = 0$, 0.1, 0.3 and 0.5 samples are shown in Fig. 2. All the samples show

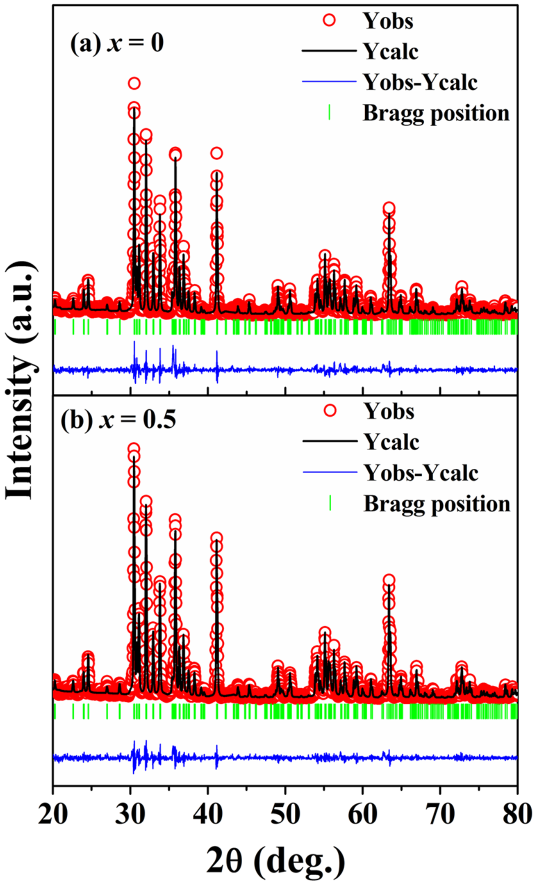

Fig. 1 XRD patterns (circles) of (**a**) $x = 0$ and (**b**) $x = 0.5$ samples along with Rietveld refined data (solid line). The dashed lines (blue) represent the difference between experimental and refined data. The (green) vertical lines show the allowed Bragg's positions. (Color figure online)

Table 1 Lattice parameters (*a* and *c*) and the spin-reorientation (Ts) and ferrimagnetic (Tc) transition temperatures of Co_2Y samples for different Mg concentrations

x	*a* (Å)	*c* (Å)	V (Å^3)	Ts (K)	Tc (K)
0	5.862	43.512	1294.8	225	613
0.1	5.861	43.502	1294.1	218	609
0.2	5.862	43.500	1294.4	209	603
0.3	5.862	43.491	1294.2	200	593
0.4	5.862	43.481	1293.9	192	585
0.5	5.863	43.479	1293.8	182	581

hexagonal plate like morphology. The porosity in the samples is found to decrease with increase in Mg concentration. The average grain sizes of all the samples were estimated by using Image J software and they are found to be in the range of 1.5–2.2 μm. The chemical composition in the samples was determined by recording EDX spectra. The typical cationic ratios of Ba:Co:Mg:Fe, for $x=0$, 0.1 and 0.3 samples are found to be 2.00:1.81:0:11.10, 2.00:1.80:0.19:11.09 and 2.00:1.41:0.59:11 respectively and they are comparable to the nominal starting compositions.

3.1 Complex impedance analysis

Impedance spectroscopy is one of the important techniques used to understand the dielectric properties, conductivity and relaxation dynamics of dielectric materials. The temperature dependence of normalized imaginary component ($Z''/Z''_{\max}$) of the impedance spectra for $x=0$, 0.1, 0.3 and 0.5 samples at different temperatures are shown in Fig. 3. For $T<383$ K, the impedance spectra are found to merge together at higher frequency ($f>10^5$ Hz) and is attributed to the possible release of space charges at the grain boundaries [23]. The impedance spectra recorded at different temperatures for various concentrations of Mg show relaxation peak at a characteristic frequency $f_{\max}$ which matches the relaxation time of charge carriers towards the applied electric field. For $x=0$ sample, the relaxation peak is observed at $f_{max}=2$ kHz at a given temperature of $T=353$ K. As the temperature is increased, the relaxation peak is found to shift towards higher frequency due to the thermal activation of relaxation and then move out of the measured frequency range. Moreover at higher temperature, especially for $T\geq 423$ K, a secondary peak is noticed in the low frequency region. For $x=0$ sample, the secondary relaxation peak is observed at $f_{max}=5$ kHz for $T=423$ K. The secondary peak is found to be suppressed and broadened with increase in Mg concentrations. The secondary peaks observed in the low frequency region can be attributed to the relaxation of charge carriers in the long range region, i.e. across the grain boundaries. Such behavior is expected at higher temperature due to the thermal activation of charge carriers. On the other hand, the primary peaks observed even at relatively low temperature can be attributed to relaxation within the short range scale, i.e. within the grains.

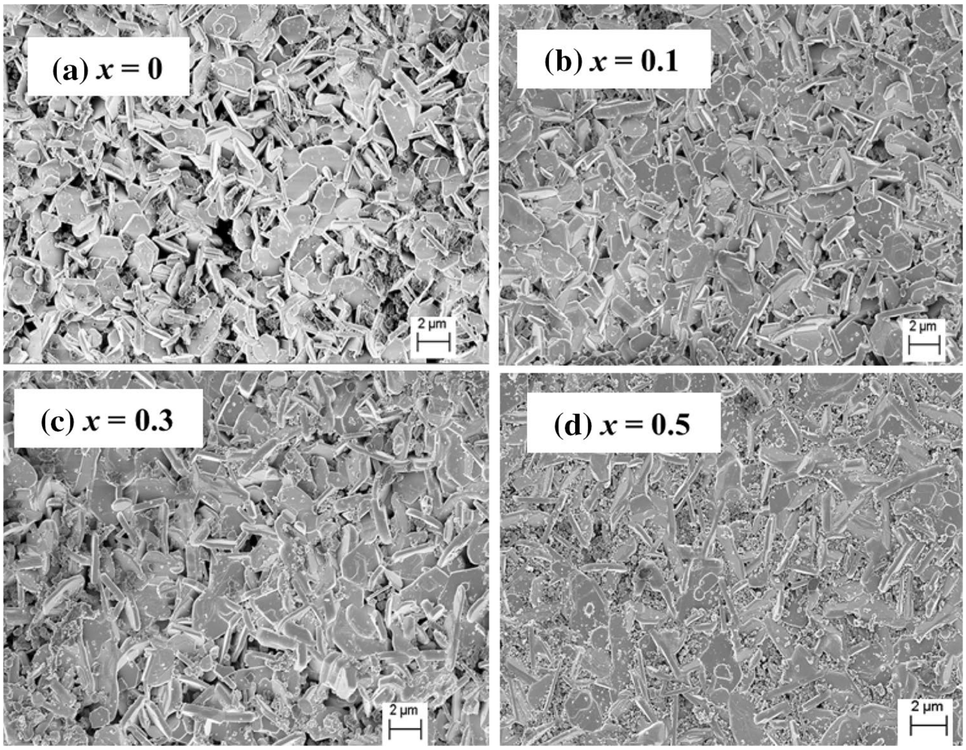

Fig. 2 FESEM micrographs of $Ba_2(Co_{1-x}Mg_x)_2Fe_{12}O_{22}$ samples for (**a**) $x=0$, (**b**) $x=0.1$, (**c**) $x=0.3$ and (**d**) $x=0.5$

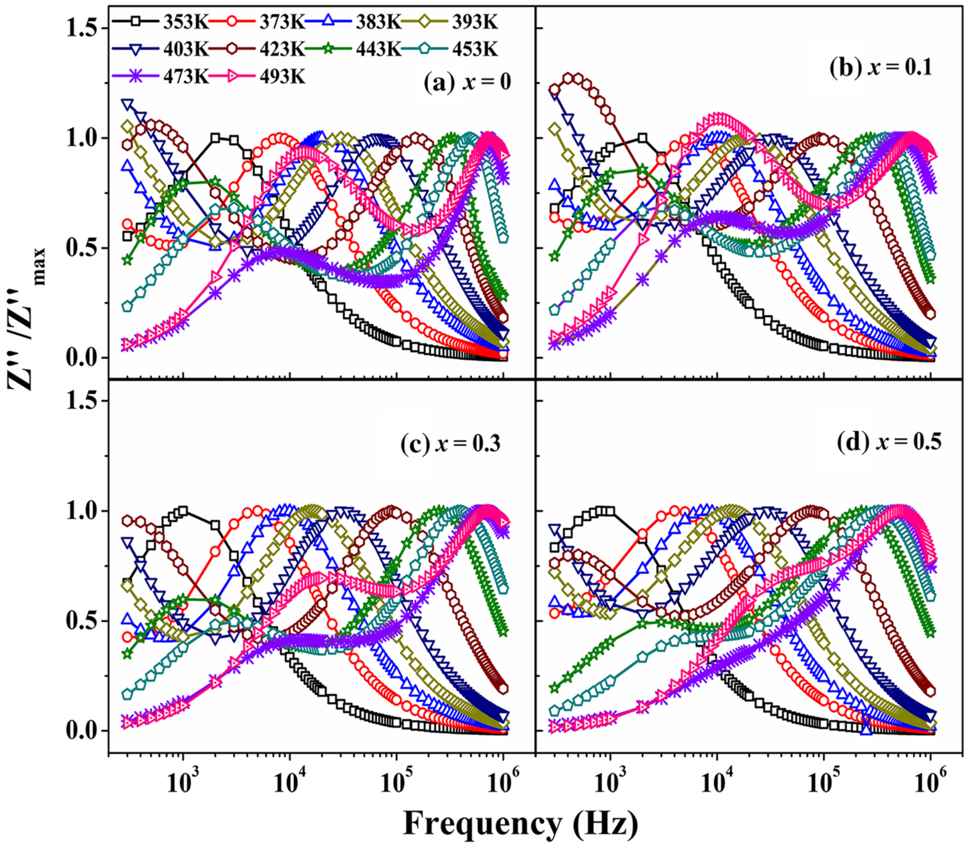

Fig. 3 Frequency dependence of normalized imaginary component of impedance spectra at different temperatures for (**a**) $x = 0$, (**b**) $x = 0.1$, (**c**) $x = 0.3$ and (**d**) $x = 0.5$ samples of Mg doped Co_2Y hexaferrite

Furthermore, in order to understand the dielectric relaxation and the nature of charge carriers responsible for the relaxation dynamics in thermally activated process, we have analyzed the temperature dependence of relaxation frequency by using the Arrhenius law [1]:

$$f = f_0 \exp\left[-\frac{E_a^z}{k_B T}\right] \tag{1}$$

here f_0 is the prefactor, k_B is the Boltzmann constant (8.617×10^{-5} eV/K) and E_a^z is the activation energy of relaxation. The plots of ln f_{max} versus T corresponding to contributions from grains and grain boundaries are shown in Fig. 4, where they all exhibit a linear behavior. The fitting of these data using the Arrhenius law (Eq. 1) by taking f_0 and E_a^z as the free parameters of the fit is shown as solid line. The E_a^z values corresponding to relaxation of charges within the grains are found to vary from 0.71 eV for $x = 0$–0.82 eV for $x = 0.5$. The corresponding E_a^z values across the grain boundaries are found to be in the range of 0.81 eV for $x = 0$–0.63 eV for $x = 0.5$.

Figure 5. shows the typical Nyquist plots (Z″ versus Z′) of $Ba_2(Co_{1-x}Mg_x)_2Fe_{12}O_{22}$ samples with $x = 0$, 0.3 and 0.5 in the temperature range of 303–623 K. A semicircular arc appears in the lower temperatures region (T ≤ 373 K) for all the samples. In polycrystalline materials, the relaxation peaks in the impedance spectra are basically due to the contributions from both grains and grain boundaries. For an ideal Debye type behavior, the center of the semicircle in the Nyquist plot should lie on the Z′ axis. In such case, the effect of grains and grain boundaries in the semicircles can be modelled by considering an equivalent circuit, where the parallel combination of RC due to grains were connected in series with that of grain boundaries. From Fig. 5, it can be seen that the center of the asymmetric semicircle lies below the Z′ axis. It reveals that the relaxation dynamics deviates from the ideal Debye type relaxation. Any deviation from the ideal Debye type relaxation in the impedance spectra can be modeled by using a constant phase element (CPE) denoted by Q. The CPE in the impedance spectra can be defined as $Z^*_{CPE} = \frac{1}{A}(j\omega)^{-s}$, where A is a constant and s represents the relaxation time distribution function ($0 \le s \le 1$). For $x = 0$ sample, at 303 K, a semicircular arc is observed as shown in Fig. 5a. The distorted nature of semicircle reveals the presence of constant phase element (CPE) in its equivalent circuit. As the temperature is increased, the arc bends towards the Z′ axis by forming a complete semicircle at around 573 K. It suggests the enhancement in the conductivity of the samples with increase in the temperature [24]. The single semicircular arc in this region corresponds to relaxation

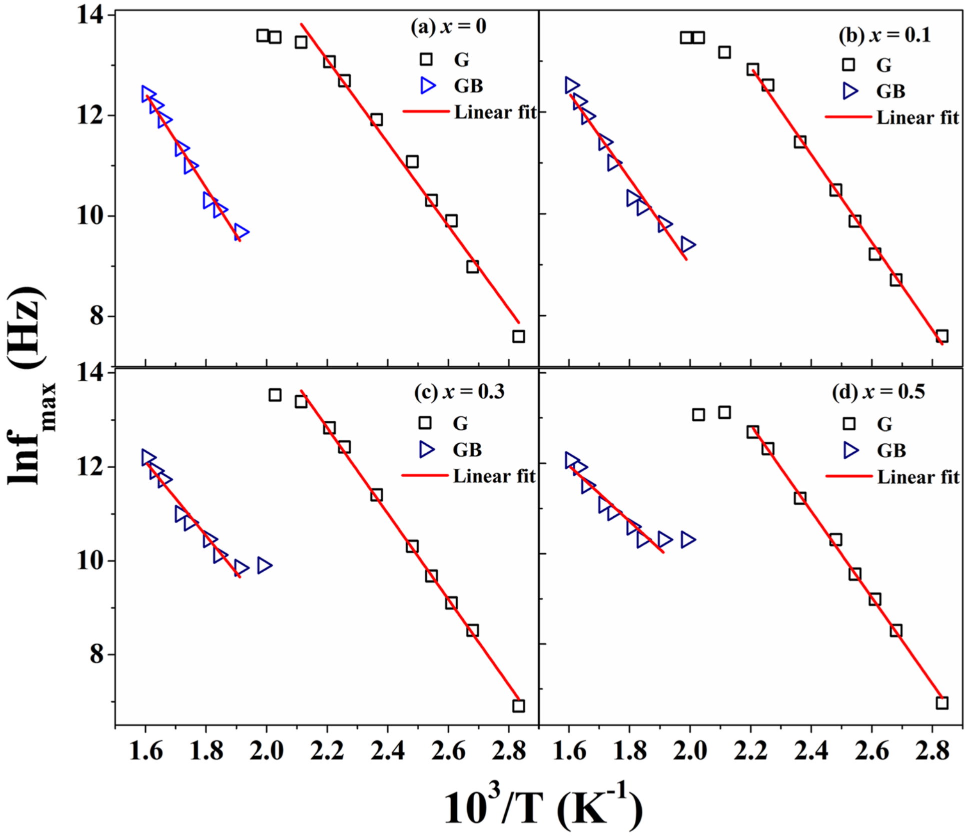

Fig. 4 Temperature dependence of relaxation frequency for (**a**) $x = 0$, (**b**) $x = 0.1$, (**c**) $x = 0.3$ and (**d**) $x = 0.5$ samples corresponding to both grains and grain boundaries contributions along with fitted data (solid line) using Arrhenius law

process at grain boundaries. An equivalent circuit comprising of parallel R_gC_g and $R_{gb}Q_{gb}$ elements connected in a series explains the Nyquist plots in the temperature range of 303–353 K (Fig. 6a) and they are attributed to the relaxation within the grains. The Nyquist plots in the high temperature region ($T \geq 573$ K) exhibit a single semicircle and could be modeled to an equivalent circuit of parallel R_gC_g and $R_{gb}Q_{gb}$ elements connected in series with electrode resistance R_{el} as shown in Fig. 6b. Here R_g and R_{gb} represent the resistance of grains and grain boundaries respectively. Whereas C_g and Q_{gb} represent the capacitance and the constant phase element associated with the grains and grain boundaries respectively. But in the intermediate temperature range of 483–523 K, a secondary asymmetric/depressed semicircular arc is observed in the lower frequency (higher Z') region as shown in Fig. 5d. These depressed semicircles gradually shifts towards lower Z' value up to 523 K and beyond that they disappear. The presence of two semicircular arcs in the intermediate temperature range reveals that the electrical response is composed of two relaxation process with different characteristic frequencies due to contributions from both grains and grain boundaries. The Nyquist plots of all other samples follow the similar behavior.

3.2 Electrical modulus analysis

Figure 7 shows the variation of imaginary part of modulus (M'') spectra with frequency at different temperatures for $Ba_2(Co_{1-x}Mg_x)_2Fe_{12}O_{22}$ samples with $x = 0$, 0.1, 0.3 and 0.5. The electrical modulus spectra exhibit peak due to relaxation of charge carriers at a characteristic frequency. The peak is found to shift towards higher frequency with increase in temperature due to thermal activation of charge carriers.

A general four parameter expression for susceptibility (M'', Z'') is proposed by Bergman [25] as :

$$M''(\omega) = \frac{M''\text{max}}{\left(\frac{1-|p-q|}{p+q}\right)\left(q\left(\frac{\omega}{\omega\text{max}}\right)^{-p} + p\left(\frac{\omega}{\omega\text{max}}\right)^{q}\right) + |p-q|} \tag{2}$$

where M''_{max} represents the imaginary part of complex modulus and ω_{max} is the corresponding peak angular frequency. Here p and q are the stretching parameters ($0 \leq p \leq 1$), ($0 \leq q \leq 1$) at low and high frequency regions respectively.

The M'' data were fitted to Bergman's 4-parameter general expression i.e., Eq. (2) and the fitted data are shown as solid lines in Fig. 7. In this case, p and q are the shape parameters at low and high frequency regions respectively. For $p = q = 1$, the relaxation process corresponds to the ideal

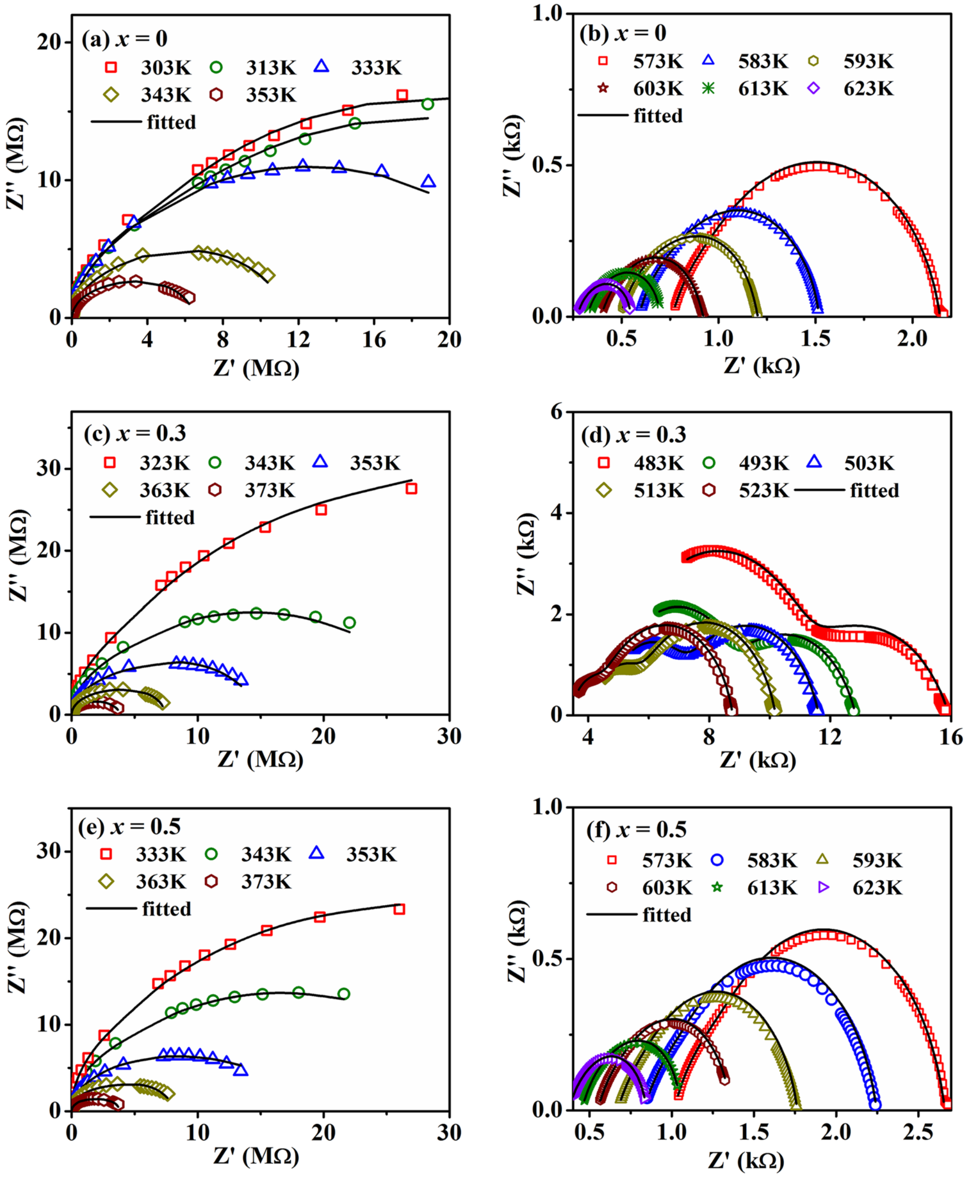

Fig. 5 Nyquist plots of complex impedance spectra of $x = 0$, 0.3 and 0.5 samples in the low temperature (**a, c, e**) and in the high temperature (**b, d, f**) regions respectively. The solid lines represent the fitted data

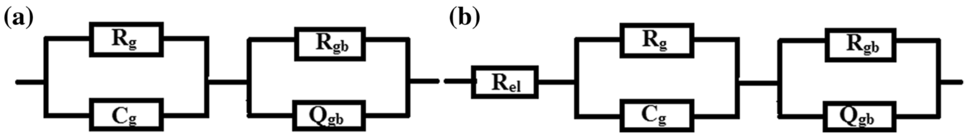

Fig. 6 Equivalent circuits used for the fitting of Nyquist plots (Z″ vs. Z′) of $Ba_2(Co_{1-x}Mg_x)_2Fe_{12}O_{22}$ samples in the low temperature (**a**) and in the high temperature (**b**) regions respectively

Debye type behavior with no interaction among the relaxation species. It is well known that the interaction strength among the relaxation species determines the shape of M″ spectra. Therefore, the knowledge of shape parameters p and q would lead to qualitative information about the interaction among the dipoles. The value of p is found to vary from 0.85 to 1 and that of q is in the range 0.73–1 for increase in temperature from 353 to 423 K. The small increase in q value signifies that the relaxing species are getting separated with increase in the temperature. It has been observed that the magnitudes of M″ spectra for different samples are comparable and a small shifting of M″ spectra towards the lower frequency is noticed with Mg substitution. But the modulus spectra are found to shift towards the higher frequency side

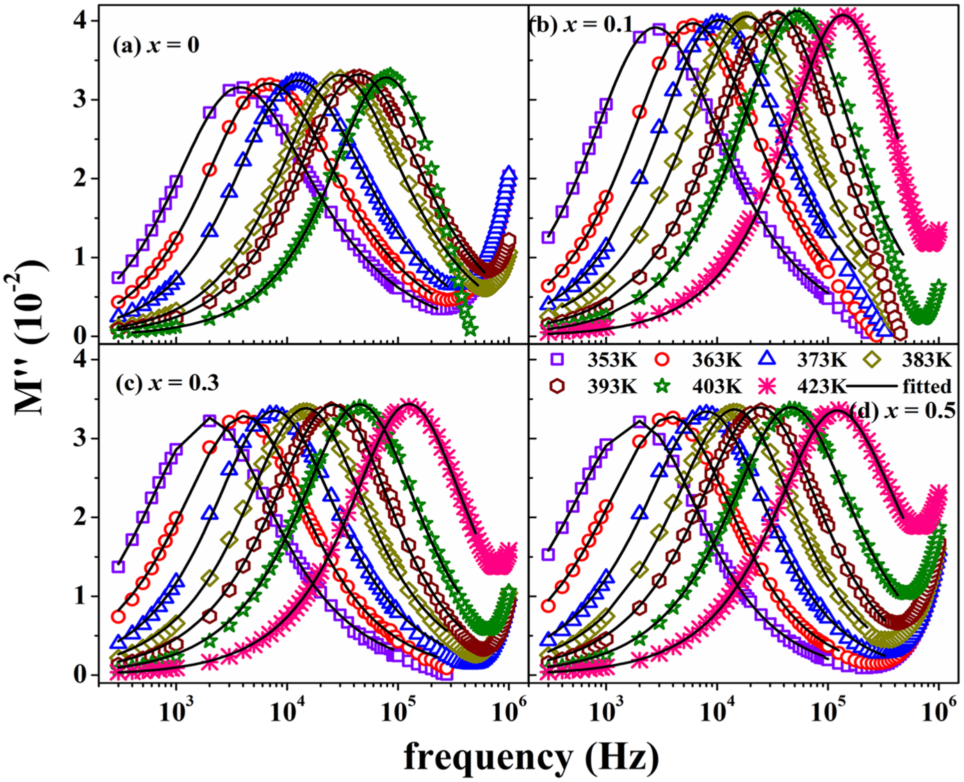

Fig. 7 Imaginary component (M″) of electric modulus as a function of frequency for (**a**) $x = 0$, (**b**) $x = 0.1$, (**c**) $x = 0.3$ and (**d**) $x = 0.5$ samples along with fitted (solid line) data using Eq. (2) at different temperatures

with increase in temperature. The peak position in the modulus spectra also provides the relaxation frequency and they can be analyzed based on Arrhenius relation: $f = f_0 \exp\left[-\frac{E_a^M}{k_B T}\right]$. From the analysis of above modulus spectra in terms of Arrhenius law, the activation energy (E_a^M) values were estimated. The plots of ln$f_{\max}$ versus T along with fitted data are shown in Fig. 8. The estimated E_a^M values are found to vary from 0.64 eV for $x = 0$–0.77 eV for $x = 0.5$. The E_a^M values are found to increase with increase in Mg concentration. It is well known that the activation energies E_a^z and E_a^M corresponding to Z″ and M'' spectra represent the localized (i.e. dielectric relaxation) and non-localized conductivity (i.e. long range conductivity) respectively. In our case, we have seen that the estimated E_a^z and E_a^M values are almost comparable with each other and it suggests that the relaxation and conduction process are governed by the same type of charge carriers [26].

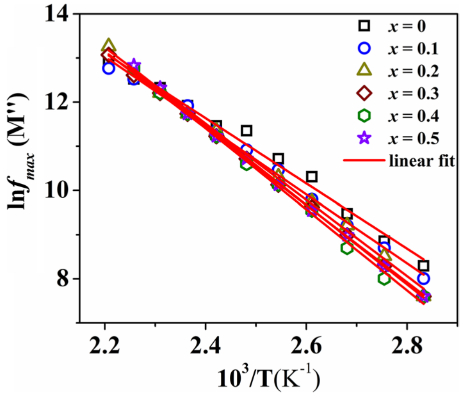

Fig. 8 Temperature dependence of relaxation frequency obtained from modulus spectra for $x = 0$, 0.1, 0.2, 0.3, 0.4 and 0.5 samples along with fitted data using Arrhenius relation

3.3 Electrical conductivity analysis

In order to further understand the electrical conductivity of Mg doped Y-type barium hexaferrite, the ac conductivity data were extracted from the experimental ε'' values using the relation [27]; $\sigma_{ac}(\omega) = \omega\, \varepsilon_0\, \varepsilon''$. Here ω represents the angular frequency of ac applied field. Figure 9 shows the frequency variation of ac conductivity at different temperatures. The ac conductivity is found to increase with increase in temperature and it suggests the negative temperature coefficient of resistance behavior. The magnitude of ac conductivity is found to decrease with increase in Mg concentration. Furthermore, the ac conductivity plot contains two different regions: one is the frequency independent plateau in the low frequency region attributed to dc conductivity due to the long-range translational motion of the charge carriers. The other one in the high frequency region increases with frequency due to increase in hopping of charge carriers. In the low temperature region, the relaxation and conductivity process are due to electron hopping between Fe^{2+} and Fe^{3+} ions

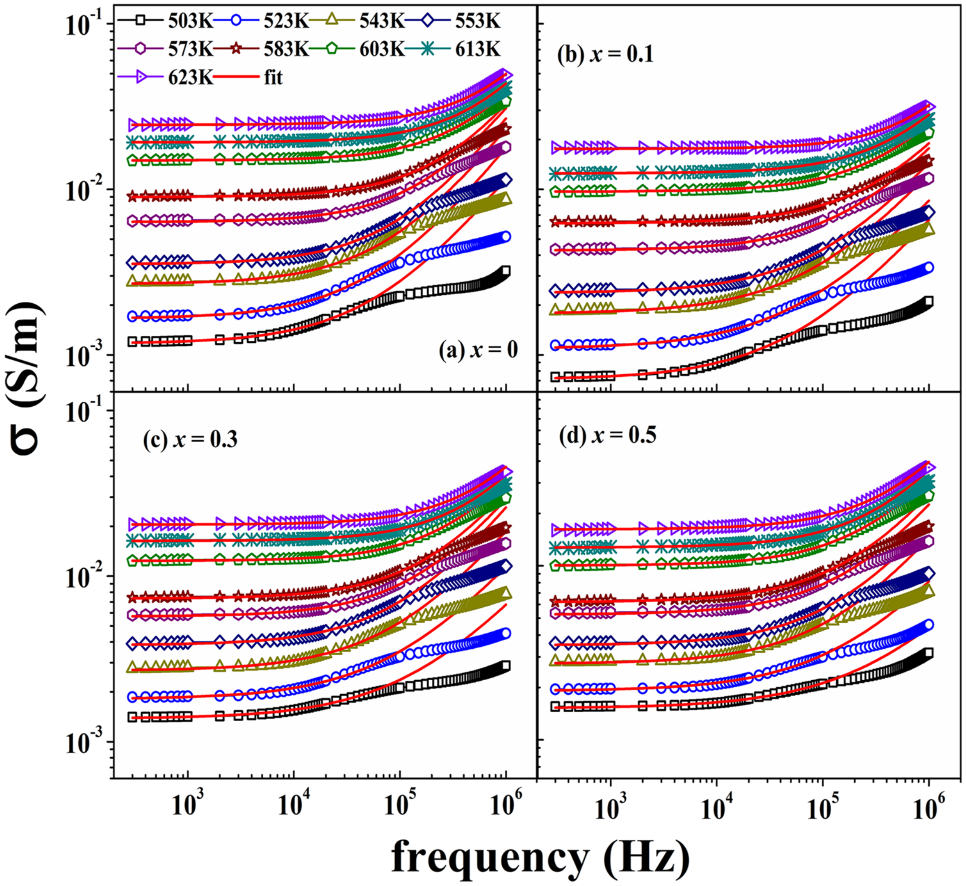

Fig. 9 (**a**–**d**) Frequency variation of ac conductivity at different temperatures along with fitted data (solid line) using Eq. (3) for $Ba_2(Co_{1-x}Mg_x)_2Fe_{12}O_{22}$ samples with $x=0$, 0.1, 0.3 and 0.5

and the hole transfer between Co^{2+} and Co^{3+} ions. Whereas at higher temperature, It is mainly due to the oxygen vacancies. In addition to that, Jump relaxation model (JRM) is one of the useful mechanism used to understand the frequency dispersion of ac conductivity at different temperatures [28]. According to JRM, two competing relaxation process takes place at higher frequency region such as (i) the unsuccessful hopping, where the jumping of ions jump back to its initial position and (ii) the successful hopping ,where the jumping ions will stay in the new site and the neighborhood ion become relaxed with respect to the jumping ions position. This characteristic feature of the conductivity as per Jonscher Power Law (JPL) [29] is given as follows:

$$\sigma'_{ac} = \sigma_0 + A\omega^{n} \tag{3}$$

here σ_0 is the dc conductivity which corresponds to plateau region in the low frequency region. The term $A\omega^n$ characterizes the dispersion phenomena, where A is a constant and n is the frequency exponent which explains the interaction among the lattice ions and the mobile charge carriers around them. The value of n basically gives the information about the nature of charge carriers. If the value of n is between $0 \le n \le 1$ then it signifies the short range motion of charge carriers. The n value will be greater than 1, if there is a localized motion of charge carriers due to back and forth movement of electrons between two charge defects [30]. Furthermore, different theoretical models have been reported to understand the temperature dependence of n values and hence the conduction process. They are (i) Quantum tunneling model, where n value is independent of temperature i.e. $n \sim 0.8$ (ii) correlated barrier hopping model, where n value decreases with increase in temperature (iii) large polaron tunneling model, where the n value decreases up to certain value then it increases and (iv) small polaron tunneling model, where the n value increases with increase in temperature [31, 32]. The values of frequency exponent, n estimated for the above samples at different temperatures are shown in Fig. 10. It can be seen that the frequency exponent n is found to increase with increase in temperature and highlights that the conduction process is controlled by small polaron tunneling model.

3.4 Magnetic properties

Figure 11a shows the magnetic hysteresis loops of $Ba_2(Co_{1-x}Mg_x)_2Fe_{12}O_{22}$ $(0 \le x \le 0.5)$ samples measured at room temperature. The magnetization measurements reveal that both the saturation magnetization (Ms) and the

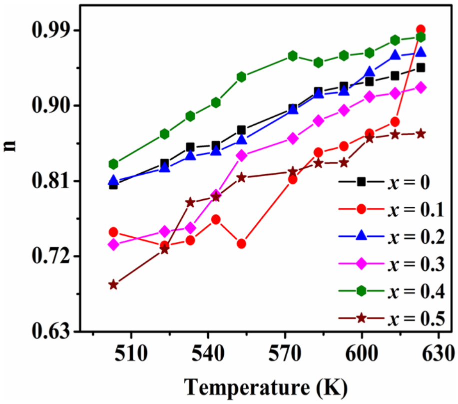

Fig. 10 Temperature variation of frequency exponent n for $Ba_2(Co_{1-x}Mg_x)_2Fe_{12}O_{22}$ samples with $x=0$ to 0.5

coercivity (Hc) values are found to decrease marginally with increase in Mg^{2+} ion concentrations. For $x=0$ sample, the saturation magnetization value is found to be 26.6 emu/g and it decreases to 22.7 emu/g for $x=0.5$ sample. The decrease in Ms values is due to the replacement of magnetic Co^{2+} ions having magnetic moment 3.88 μ_B per ion by a non-magnetic Mg^{2+} ions [33]. Furthermore, the coercvity is also found to decrease with increase in Mg^{2+} ion concentration. Since the Co^{2+} ions have large magnetic anisotropy than that of Mg^{2+} ions, the substitution of Co^{2+} ions by Mg^{2+} ions causes the reduction in magneto-crystalline anisotropy constant and this leads to decrease in coercivity.

In order to further understand the magnetic properties, the temperature dependence of magnetization of $Ba_2(Co_{1-x}Mg_x)_2Fe_{12}O_{22}$ hexaferrites were measured under zero field cooled mode for H = 100 Oe. Figure 11b shows the magnetization versus temperature (M–T) plots for different concentrations of Mg in Co_2Y hexaferrite. It is noticed that all the samples exhibit two magnetic transitions i.e. ferrimagnetic transition at Tc followed by hellimagnetic transition (Ts) at low temperature. These types of transitions have been observed in Zn, Ni and Sr doped Y-type hexaferrites [7, 8, 21]. Both Tc and Ts values were determined from the inflection points, i.e. corresponding to valley and peak positions of dM/dT versus T plots. For $x=0$ sample, the Tc and Ts values are found to be 613 K and 225 K respectively. These values for other samples are given in Table 1. It is found that both Tc and Ts values decrease with increase in Mg^{2+} ion concentrations. Generally, in ferrite materials, the Tc value depends upon the thermal stability of a spin alignment and the spin alignment strongly depends upon the super-exchange interaction between metal ions at two magnetic sub-lattices. Therefore, the decrease in Tc values can be attributed to the weakening of super-exchange interaction due to occupation of non-magnetic Mg^{2+} ions at the octahedral sites of magnetic Co^{2+} ions. In addition to that, the decrease in Ts value could be due to the decrease in

Fig. 11 (**a**) Magnetic hysteresis loops at room temperature, (**b**) Temperature variation of magnetization (M) normalized to magnetization measured at 300 K (M_{300}) for $Ba_2(Co_{1-x}Mg_x)_2Fe_{12}O_{22}$ and (**c, d**) Both ZFC and FC magnetization measured from 30 to 300 K for $x=0$ and 0.5 samples

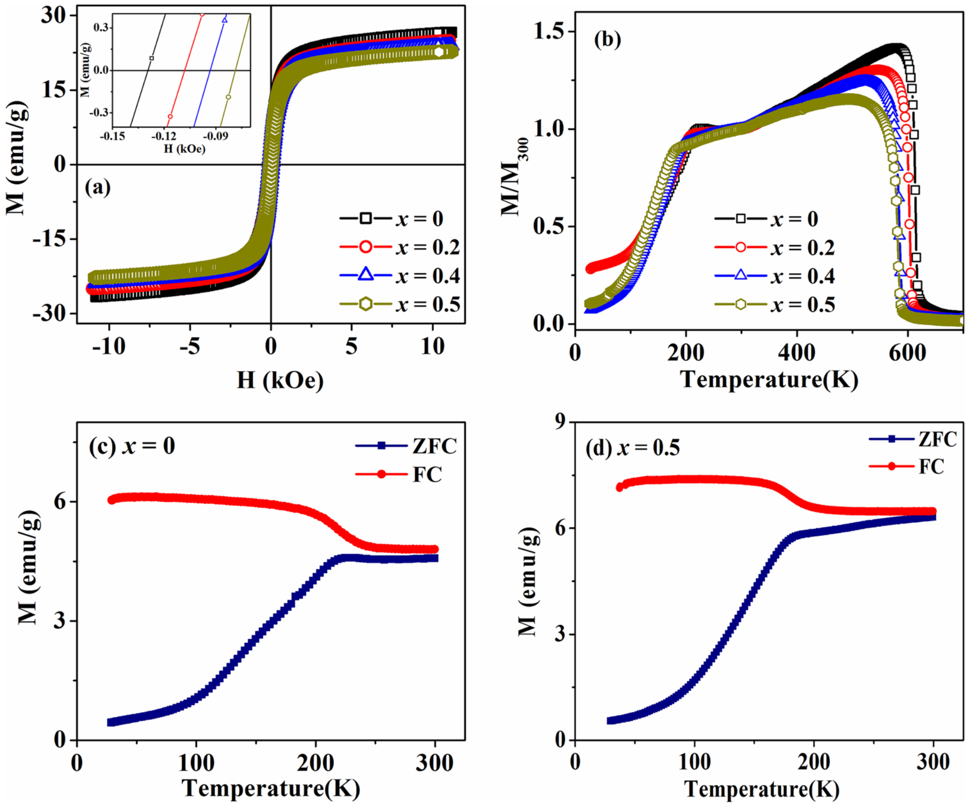

magnetic anisotropy due to Mg^{2+} ion substitution. Further to get more information about magnetic interactions at low temperatures, the magnetization measurements were carried out in both zero field cooled (ZFC) and field cooled (FC) mode at 100 Oe for $x = 0$ and 0.5 samples in the temperature range of 30–300 K as shown in Fig. 11c, d. Below the helimagnetic spin-eorientation transition temperature (Ts), a large irreversibility is seen between ZFC and FC curves. Such irreversibility is expected for T < Ts [34].

4 Conclusions

Polycrystalline $Ba_2(Co_{1-x}Mg_x)_2Fe_{12}O_{22}$ ($0 \le x \le 0.5$) samples were prepared in single phase form by solid state reaction method and they are found to be crystallized into rhombohedral structure with R-3m space group. The lattice constant *c* is found to decrease systematically with increase in Mg concentration. The asymmetric and depressed semicircular arc in complex impedance spectra reveals that the relaxation of charge carriers deviates from ideal Debye type behavior. The analysis of ac conductivity data shows that it is governed by the small polaron model. The M–H measurements show that both Ms and Hc values are found to decrease with increase in Mg concentration. The temperature dependence of magnetization data show two magnetic transition temperatures corresponding ferrimagnetic and helimagnetic spin-reorientation transitions. Both Tc and Ts values are found to decrease with increase in Mg^{2+} ion concentration. The decrease in Tc value signifies the weakening of superexchange interaction and the decrease Ts value is attributed to the decrease in magnetic planar anisotropy.

Acknowledgements Authors are thankful to Central Instrument Facility (CIF), IIT Guwahati for extending FESEM facility.

References

1. A.M. Abo El Ata, S.M. Attia, J. Magn. Magn. Mater. **257**, 165 (2003). https://doi.org/10.1016/S0304-8853(02)00446-8
2. S. Kamba, V. Goian, M. Savinov et al., J. Appl. Phys. **107**, 104109 (2010). https://doi.org/10.1063/1.3402379
3. S.H. Mahmood, F.S. Jaradat, A.F. Lehlooh, A. Hammoudeh, Ceram. Int. **40**, 5231 (2014). https://doi.org/10.1016/j.ceramint.2013.10.092
4. M. Ahmad, Q. Ali, I. Ali et al., J. Alloy. Compd. **580**, 23 (2013). https://doi.org/10.1016/j.jallcom.2013.05.076
5. C.A. Stergiou, G. Litsardakis, J. Magn. Magn. Mater. **405**, 54 (2016). https://doi.org/10.1016/j.jmmm.2015.12.027
6. A. Deriu, F. Licci, S. Rinaldi, T. Besagni, J. Magn. Magn. Mater. **22**, 257 (1981). https://doi.org/10.1016/0304-8853(81)90030-5
7. J.T. Lim, C.S. Kim, IEEE Trans. Magn. **49**, 4192 (2013)
8. K.L. Cho, C.S. Kim, IEEE Trans. Magn. **49**, 4291 (2013). https://doi.org/10.1109/TMAG.2013.2243125
9. T. Kouji, A. Nobuyuki, O. Shintaro, U. Hiroshi, A. Taka-hisa, Appl. Phys. Express **1**, 031301 (2008)
10. T. Kimura, G. Lawes, A.P. Ramirez, Phys. Rev. Lett. **94**, 137201 (2005)
11. G. Wang, S. Cao, Y. Cao et al., J. Appl. Phys. **118**, 094102 (2015). https://doi.org/10.1063/1.4929956
12. M.X. Wu, W.J. Zhong, X.S. Gao, L.J. Liu, Z.W. Liu, J. Appl. Phys. **116**, 224103 (2014). https://doi.org/10.1063/1.4903835
13. S. Hirose, K. Haruki, A. Ando, T. Kimura, Appl. Phys. Lett. **104**, 022907 (2014). https://doi.org/10.1063/1.4862432
14. S. Hirose, K. Haruki, A. Ando, T. Kimura, J. Am. Ceram. Soc. **98**, 2104 (2015). https://doi.org/10.1111/jace.13573
15. M. Costa, G.P. Junior, A. Sombra, Mater. Chem. Phys. **123**, 35 (2010)
16. Y.A. Farzin, O. Mirzaee, A. Ghasemi, J. Magn. Magn. Mater. **371**, 14 (2014)
17. R.A. Khan, S. Mizukami, A.M. Khan, B. Ismail, A.R. Khan, T. Miyazaki, J. Alloy. Compd. **637**, 197 (2015)
18. R.A. Khan, S. Mir, A.M. Khan, B. Ismail, A.R. Khan, Ceram. Int. **40**, 11205 (2014)
19. R.A. Young, *The Rietveld Method. International Union of Crystallography*. (Oxford University Press, Oxford, 1993)
20. M. Zhang, J. Dai, L. Yin et al., J. Alloy. Compd. **689**, 75 (2016). https://doi.org/10.1016/j.jallcom.2016.07.318
21. M.H. Won, C.S. Kim, J. Appl. Phys. **115**, 17A509 (2014). https://doi.org/10.1063/1.4860939
22. R.D. Shannon, Acta Crystallogr. A **32**, 751 (1976)
23. R. Tang, C. Jiang, W. Qian et al., Sci. Rep. **5**, 13645 (2015). https://doi.org/10.1038/srep13645
24. Y.J. Wong, J. Hassan, M. Hashim, J. Alloy. Compd. **571**, 138 (2013). https://doi.org/10.1016/j.jallcom.2013.03.123
25. R. Bergman, J. Appl. Phys. **88**, 1356 (2000). https://doi.org/10.1063/1.373824
26. M.M. Costa, G.F.M.P. Júnior, A.S.B. Sombra, Mater. Chem. Phys. **123**, 35 (2010). https://doi.org/10.1016/j.matchemphys.2010.03.026
27. S. Pattanayak, B.N. Parida, P.R. Das, R.N.P. Choudhary, Appl. Phys. A **112**, 387 (2013). https://doi.org/10.1007/s00339-012-7412-6
28. B. Deka, S. Ravi, A. Perumal, D. Pamu, Ceram. Int. **43**, 1323 (2017). https://doi.org/10.1016/j.ceramint.2016.10.087
29. A.K. Jonscher, Nature **267**, 673 (1977)
30. S. Khadhraoui, A. Triki, S. Hcini, S. Zemni, M. Oumezzine, J. Magn. Magn. Mater. **371**, 69 (2014). https://doi.org/10.1016/j.jmmm.2014.07.044
31. S. Nasri, M. Megdiche, M. Gargouri, Ceram. Int. **42**, 943 (2016). https://doi.org/10.1016/j.ceramint.2015.09.023
32. R. Gangopadhyay, A. De, S. Das, J. Appl. Phys. **87**, 2363 (2000). https://doi.org/10.1063/1.372188
33. Y. Alizad Farzin, O. Mirzaee, A. Ghasemi, J. Magn. Magn. Mater. **371**, 14 (2014). https://doi.org/10.1016/j.jmmm.2014.07.007
34. A. Alsmadi, I. Bsoul, S. Mahmood et al., J. Appl. Phys. **114**, 243910 (2013)